Rijksuniversiteit Groningen

Bachelor Thesis

Constraining Formation Parameters of M33 using Chemical Evolution Model RAMICES II

Author:
J.J. Wubben
S4895738

Supervisors:
F. Fraterneli
J.K.S. Friske

Contents

1 Introduction

The chemical composition of galaxies is ever-changing. The evolution of the composition plays a key role in shaping the observable properties of galaxies. Modeling chemical evolution enables us to connect star formation, gas flows, and feedback to observed abundance trends across cosmic time. Therefore, understanding chemical evolution is essential for interpreting the formation and structural development of galaxies.

Efforts to lay the theoretical groundwork of chemical evolution in galaxies date back to the 1940s and 1950s, when Hoyle suggested that elements heavier than helium were created in stars (Hoyle 1946, 1954). Before that, only the fusion of hydrogen into helium had been explored (Bethe, 1939), and the production of heavier elements in stars was merely a suggestion (Eddington, 1920). The study of nucleosynthesis reached a milestone when Burbidge et al. (1957) showed that, with the addition of neutron capture to the existing theory, stars can form nearly all elements in the periodic table, therefore introducing stars as the principal site of chemical enrichment. The formulation for the rate of star formation started in the same year when van den Bergh (1957) considered that the decrease in the density of interstellar gas could be caused by star formation. With that hypothesis, Schmidt (1959) came up with a relation between gas density and the star formation rate that is still used today. With this relation, the stellar scale element production can be connected to properties on a galactic scale, such as the star formation history. This was first demonstrated by Tinsley (1979), who was able to constrain large scale galactic properties based on models for chemical evolution.

Today, it is generally agreed upon in galactic chemical evolution that galaxies follow an “open box" model, rather than a “closed box" model, though this was not always the case. In the closed box model, a galaxy is a closed system that cannot interact with the circumgalactic medium (CGM) or intergalactic medium. This caused a number of disconnections between models and observations. The first issue was the G-dwarf problem Pagel (1997), where we observe too many low-metallicity stars in the Solar vicinity. This was found to not only happen in the Milky Way, but was also encountered in external galaxies, like M31 (Worthey et al., 1996). Another problem is that the gas of the galaxy alone cannot sustain star formation in the long term (Larson et al., 1980). The solution to this is accretion of gas from the intergalactic or circumgalactic medium onto the star forming galactic disc (Tinsley, 1979). Mayor & Vigroux (1981) showed how accretion of gas with a smaller angular momentum drives inward radial motions into the disc. They found that an infall model neglecting radial motions leads to physically inconsistent results. A model with radial motions was found to produce abundance gradients in better agreement with observations. The infall rate and radial flows are described by initial conditions and cosmological physics laws, but due to uncertainties in current cosmological simulations they are not well constrained.

There are still many uncertainties in the formation of galaxies, such as the mass distribution of new-born stars (Kroupa 2001; Chabrier 2003), rotational velocity of the CGM (Hodges-Kluck et al., 2016), and the chemical abundance of heavy elements (Côté et al., 2019), leading to a large parameters space for chemical evolution models. By exploring the chemical evolution of M33, this thesis aims to constrain some of those. For this, we chose the Radial Migration Chemical Evolution Simulation (hereafter RAMICES II) developed by Fraser-Govil (2022). RAMICES II is a spatially resolved, thermally-phased simulational model for galactic chemical evolution. Using a two-phase interstellar medium (ISM), realistic yields, and separate parameterizations for

the global infall rate and induced radial flows, RAMICES II reproduces the underlying physics of chemical evolution, as we try to uncover parameters essential in the formation of M33.

M33 (NGC 598) has been the subject of many chemical evolution studies. It is a low-luminosity spiral galaxy of type SA(s)cd (de Vaucouleurs et al., 1991) located in the Local Group, at a distance of 840 kpc (Freedman et al., 1991). M33 has an angular size of $28'$ and a relatively low inclination of 54° (Zaritsky et al. 1989; Kam et al. 2015). Because of this position, we are able to observe individual regions and distinguish origins of abundance measurements, making M33 an ideal candidate for chemical evolution modeling, combined with the fact that this galaxy shows no signs of recent mergers and no presence of a prominent bulge and bar component (Regan & Vogel, 1994).
M33 is believed to be $\sim$ 10Gyr old, based on the age of the oldest star clusters (Ma et al., 2002). Magrini et al. (2007a) determined the star formation rate for two time intervals. Based on planetary nebulae, they derived that in recent times (1-4 Gyr ago), M33 had a mean star formation rate of $0.55 M_{\odot}\mathrm{yr}^{-1}$, and when looking at a larger time interval (1-8 Gyr ago), the mean star formation rate increases to $1.1 M_{\odot}\mathrm{yr}^{-1}$. Ferguson et al. (2007) studied the surface brightness of M33 and identified a break in the exponential profile around $\sim$ 8kpc, which suggests that the stellar disc ends there (van der Kruit & Searle, 1981). The scale length of the stellar disc was found to be 1.4 kpc (Regan & Vogel, 1994), but the total gas scale length is hard to identify. Molecular hydrogen has a scale length of 1.9 ± 0.1 kpc, with a surface density of $\Sigma_{\mathrm{H}_2} = 8.5 \pm 0.2 M_{\odot}\mathrm{pc}^{-2}$ in the central kpc, while the surface density of atomic hydrogen stays constant at $\Sigma_{\mathrm{HI}} = 6 \pm 2 M_{\odot}\mathrm{pc}^{-2}$ for at least 8.5 kpc, making it hard to identify a scale length (Gratier et al., 2010). The total baryonic mass of M33 is made up of a stellar component, believed to be $3.2 \pm 0.4 \times 10^9 M_{\odot}$, and a gas component, of roughly $\sim 3.2 \times 10^9 M_{\odot}$ (van der Marel et al. 2012; Corbelli 2003).

Diaz & Tosi (1984) were among the first to attempt the chemical evolution of M33. This study did not gain any real insights into the origin of M33, as the infall rate and the star formation rate in this model were not supported by astrophysical theories. Mollá et al. (1997) used a model developed by Ferrini & Poggianti (1993) to obtain the time evolution of the oxygen gradient in M33 by adding a radial dependence to the infall rate and star formation rate. As radial gas profiles and the metallicity determinations in stellar populations of different ages became available, the models were reconsidered by Magrini et al. (2007a). They found that a model with an infall rate that is almost constant over time reproduced the observed abundances best. Kang et al. introduced a model that calculates the evolution of the atomic and molecular gas separately based on a molecular-hydrogen-correlated star-formation law. With this model, they found that the outflow rate could be linked to the star formation rate (Kang et al. 2012, 2023).

In this thesis we will use RAMICES II to model the chemical evolution of M33 to gain new insights into the formation of this galaxy, as we explore slightly different formation scenarios, explicitly modeling the effect of angular momentum-driven radial flows. Section 2 will cover all the events that change the chemical composition of a galaxy, and Section 3 describes how these are incorporated in the model. The findings of the model will be compared with observed abundances in M33. These will be introduced in Section 4. Section 5 presents the parameters of the fiducial fit and compares the metallicity gradient produced by RAMICES II to the observational data. In Section 6 we discuss some limitations and improvements for this work. The final conclusions will be drawn in Section 7.

2 Chemical Evolution

Many different processes play a role in the galactic chemical composition and changing thereof. In order to understand how various elements are formed and distributed, we will examine these processes step by step. The start of this cycle is marked by star formation, followed by the transformation of elements through nuclear fusion within stars and their remnants. These products are released into the ISM through stellar death and remnants events. Finally, we will look into the gas streams in and out of the galaxy and their impact on the chemical composition. All of the material in this section has previously been discussed by Burbidge et al. (1957) and Friske (2024).

2.1 Star Formation

Stars produce elements and change the abundance of their surrounding ISM. Before they can do that, they first have to be formed. This happens when clouds of gas have a large mass, causing the clouds to collapse under their own gravitational pull. This process happens mainly in cold regions with large density and low pressure. Collapsed clouds require a minimum mass of $0.08 M_\odot$ to start the fusion of hydrogen. When this has started, the cloud can be referred to as a star.
The rate at which gas is converted into stars is an important contributor to the chemical evolution of a galaxy. After the initial relation formulated by Schmidt (1959), Kennicutt (1998) found a relation between the surface densities of stars and gas, instead of using volume density,

$$\dot{\Sigma}_* \propto \Sigma_{\text{gas}}^n \tag{1}$$

This power law breaks down at very high and low densities. At high densities, the star formation rate cannot increase to rates as high as described by the power law. These densities are not reached in M33, therefore we will not explore this rephrasing. At low surface densities, star formation is suppressed as gas clouds cannot gravitationally collapse to form stars. Such low densities do occur in M33, therefore a modified version of the Schmidt-Kennicutt law will be implemented in our research.
From the change in stellar surface density, the star formation rate per area SFR can be derived,

$$\text{SFR} = A\dot{\Sigma}_* \tag{2}$$

with A as the surface area.
This rate does not produce the amount of stars formed per time, but the stellar mass formed per time ($M_\odot \text{pc}^{-2}$). This is because the mass of the formed stars is not distributed uniformly. The amount of stars created per mass interval is described by the Initial Mass Function (IMF). The first IMF, observed by Salpeter (1955), was a power law

$$\frac{dN}{dm} \propto m^{-\alpha} \tag{3}$$

where N is the number density and the exponent was found to be $\alpha = 2.35$. Other forms for the IMF have been proposed (Kroupa 2001; Chabrier 2003), and most are based on the Salpeter power law, but there is no universal IMF. It is also not precisely known which function M33 follows. The uncertainty here lies in the unobservability of the IMF. The IMF describes the distribution of stellar masses at birth, but the stars we observe today have evolved since their formation, and many heavy stars have already died by the time we observe the stellar population. Moreover, the distance to external galaxies complicates efforts to observe individual stars in the galaxy.

2.2 Stellar Nucleosynthesis

During the lifetime is a star, hydrogen is fused into helium in the core of the star. This is a process that happens in all stars, regardless of their mass. When most hydrogen in the core is burned up and turned into helium, the pressure of the core, where the hydrogen-burning takes place, decreases and can no longer counteract the gravitational pressure of the star, therefore the core contracts. The contraction of the core leads to an increased density, temperature, and pressure in the inner region. The increase in pressure stops the contraction. The higher the mass of the star, the more the temperature of the core increases during the contraction. That is the reason why the following steps of stellar evolution depend heavily on the mass of the star.
The lifetime of stars is related to their mass. Low-mass stars live longer than high-mass stars. This is due to the fact that low-mass stars do not deplete their hydrogen as fast. Hydrogen-burning takes significantly more time than all the other burning phases a star can undergo. Therefore, the lifetime of a star is approximated by the time it takes the star to burn most of its hydrogen supply, which goes as

$$\tau_{\text{H-burning}} \sim 10 \left(\frac{M}{M_\odot} \right)^{-2.5} \text{Gyr} \tag{4}$$

Very low-mass stars ($M \lesssim 0.5 M_\odot$) only undergo hydrogen-burning, and never reach the temperature necessary for helium-burning. Stars with a mass below $1.5\text{M}_\odot$ do not reach the density necessary for helium burning before the core has contracted to the point it becomes degenerate. The core density can no longer increase due to the Pauli exclusion principle Pauli (1925), but its temperature keeps increasing until the critical temperature is reached. A sudden and explosive start of helium fusion takes place, which is referred to as the helium flash. The energy released in the process lifts the core out of degeneracy, and a helium-burning core surrounded by a hydrogen-burning shell is left. Stars with a mass above $1.5\text{M}_\odot$ reach the critical temperature for helium fusion without becoming degenerate.
For heavier stars, this process repeats multiple times with different elements. One element is fused into a heavier element in the core, until the core is exhausted of its supply of that element. That is when the core contracts again until it reaches a temperature sufficiently large to start the fusion of the next element. This continues until ^{56}Fe. Iron is the heaviest stable element that is produced during stellar nucleosynthesis. There are some more elements similar to ^{56}Fe produced in stellar nucleosynthesis, which are called the iron peak elements. They are created in the silicone-burning phase, which is the last nucleosynthesis phase. Many of the iron-peak elements are unstable isotopes that decay back into ^{56}Fe.
For all the previously created elements, energy was released during the process, whereas the fusion of elements heavier than iron is an endothermic process: it requires more energy than is released. Iron is created in stars with a minimum mass of $8\text{M}_\odot$.

2.3 Stellar death

The path of stellar death stars undergo depends heavily on their mass. Below, I will explain the scenarios that take place once stars reach the end of their stellar lifetime (Friske, 2024).

AGB events

The low to intermediate mass stars, up until $\sim 8 M_\odot$, do not go supernova. Instead once energy in the core is depleted after the helium flash has taken place, the core contracts again, while the total radius increases. The star becomes a giant, and events related to the star will from now on

be referred to as AGB (asymptotic giant branch) events, after its location on the Hertzsprung-Russell diagram. The contraction of the core does not increase the temperature sufficiently to start the fusion of a next element. The core becomes degenerate, and the pressure of free electrons eventually stops the contraction. In the center, a white dwarf starts forming. While the core contraction has stopped, the expansion of the outer regions has not, and a lot of mass is ejected in the form of stellar wind. What is left, is a planetary nebula with a white dwarf at its center.
The most abundant element in a white dwarf depends on whether the progenitor star went through helium-burning. As the lifetime of low-mass stars that do not reach helium-burning is longer than the Hubble time, majority of white dwarfs largely consist of carbon and oxygen.
Stars that die this way are not massive enough to reach the production of iron. The heavier stars in this range are able to undergo carbon-burning and form oxygen and neon. The gas released through AGB events can therefore be rich in helium, carbon, oxygen, and neon. During AGB events, elements heavier than iron are also released in small amounts. This will be discussed in section 2.5.

Core-Collapse Supernovae
High-mass stars ($M_\star > 8M_\odot$) go through the fusion of hydrogen, helium, carbon, neon, oxygen, and silicone in order to produce iron. At the end, all of these processes are happening at the same time in different shells. Each burning phase lasts shorter than the previous one, as the core temperature increases, so does the nuclear reaction rate. At the end of the silicone-burning phase, the core consists of iron. This iron cannot be fused into higher elements without needing energy to start the process. As energy in the core is depleted, the core contracts, and is not stopped by the next fusion-phase. The core is now electron degenerate, but after reaching the Chandrasekhar limit of $\sim 1.4M_\odot$ (Chandrasekhar, 1931), the degeneracy pressure cannot stop the contraction anymore, and the core collapses. During this collapse, the temperature reaches a value large enough to create photons that can destroy the iron nuclei in the center of the star. The photodisintegration causes a chain of reactions, until the core only consists of protons, neutrons, and free electrons. At a sufficiently large density, even the protons and free electrons fuse into neutrons

$$p + e^- \rightarrow n + \nu_e \ .$$

Neutrons are fermions, which obey Pauli's exclusion principle. The neutron degeneracy pressure increases again and counteracts the gravitational pressure, finally stopping the collapse. The core rebounds, which produces a shock that travels through all the layers of the star and triggers a supernova where the outer layers of the star are violently ejected into the surrounding space. This is called a core-collapse supernova (ccSN).
This collapse of the core creates a neutron star. If the neutron star has a mass above $3M_\odot$, it will collapse into a black hole.

The ejected gas is still rich in iron. That is because not all iron is destroyed during photo-disintegration. Only the iron nuclei in the most central region are destroyed, but outside of that region, the iron survives. In addition to iron, the ccSNe eject the elements in the other shells, with many so-called α-elements (O, Ne, Mg), that are named after the process to create them: the addition of an α-particle or $^4_2$He-nucleus to a pre-existing element.

Electron Capture Supernovae
Some intermediate-mass stars ($\sim 8M_\odot$) walk a slightly different path to stellar death. The stars in this mass region are not yet massive enough to start iron fusion in its core. Instead, the core

is filled with oxygen, neon and magnesium. During contraction, the core becomes degenerate and reaches a temperature for electron capture to happen. This reduces the pressure and causes the core to collapse and trigger a supernova. These events are referred to as electron capture supernovae (ecSNe). The gas ejected during ecSNe has roughly the same abundance as that of a ccSN, but is not as rich in iron (Jones et al. 2019; Wanajo et al. 2010).

2.4 Remnant Events

Supernovae type Ia

Low-mass star deaths result in white dwarfs. That is the starting point for supernovae of type Ia (SNIa) to develop. There are multiple scenarios that will end in a SNIa, and here we discuss the two most common ones. All scenarios consider a white dwarf that is part of a binary system. One of its possible binary companions is a star in the hydrogen-burning phase. At the end of this star's lifetime, it will increase in size and become a giant star. If the size increases such that it exceeds the Roche-Lobe limit, it will start transferring gas to the white dwarf. As the Chandrasekhar limit of $\sim 1.4 M_\odot$ is reached, the white dwarf is no longer stable and it explodes into a SNIa. At this point, the density in the white dwarf becomes large enough to resume the fusion process. Quickly, all the carbon and oxygen is fused into iron. This is immediately released in the SNIa. The ejected gas does not contain any hydrogen or helium, and is very rich in iron.

If the white dwarf's binary companion is another white dwarf, it is only possible for an SNIa to take place if the combined mass of the dwarfs exceeds the Chandrasekhar limit. Over the course of the evolution of the binary system, the dwarfs spiral inward and eventually merge. If the Chandrasekhar limit is exceeded, this merge triggers an explosion. The SNIa leaves no remnant, and all gas is fed back to the galaxy.

Neutron Star Merger

Neutron star merger events (NSM) start with neutron stars left over from ccSNe. When two neutron stars are in a binary system, they can spiral inwards and eventually merge. The merge triggers a violent explosion that releases neutron-rich material.

These merger events themselves do not change the abundance of the surrounding ISM significantly, as most of the released material consists of neutrons, not atoms. Still, they are important and are the main production site of heavy elements due to their high pressure and density.

2.5 Production of heavier elements

While stellar nucleosynthesis does not produce elements heavier than iron, those elements are observed in the Universe. These heavy elements form in a process called neutron-capture, first described by Burbidge et al. (1957), which can happen either slowly (s-process) or rapidly (r-process), but the mechanism works the same on both timescales.

In certain high density environments with sufficiently high neutron fluxes, an atom can capture a neutron. This forms an isotope of the same element, but has a mass number that is increased by one. If the created isotope is unstable and the half-life time is shorter than the neutron-capture timescale, the isotope decays. This happens by β^- decay,

$$n \rightarrow p + e^- + \bar{\nu_e} \ ,$$

where a neutron is turned into a proton. The β^- decays happen until a stable nucleus is reached. Now, the nucleus has more time to capture another free neutron.

The s-process
The s-process happens over thousands of years in AGB-phase stars. Intermediate and strongly rotating heavy AGB stars have a density sufficiently large for free neutrons to be captured. This capturing is usually done by an iron(-peak) seed that was left from a supernova of a previous stellar generation.
The main sources of neutrons in AGB stars are carbon and neon, which are produced during fusion, as discussed in Section 2.2. The reactions happen as follows:

$$^{13}_{6}\mathrm{C} + ^{4}_{2}\mathrm{He} \rightarrow ^{16}_{8}\mathrm{O} + n \text{ , and}$$

$$^{22}_{10}\mathrm{Ne} + ^{4}_{2}\mathrm{He} \rightarrow ^{25}_{12}\mathrm{Mg} + n \text{ .}$$

Because the timescale for this process is very large, it is more likely that an unstable isotope will decay before it can capture another free neutron. This makes it so that all unstable nuclei that are created in this process are very close to the so-called valley of stability.

The r-process
Most of the heavier elements are produced in the r-process, which happens at a shorter timescale than the s-process. In NSM explosions, atoms can quickly capture many free neutrons. The timescale of neutron-capture in NSMs is much shorter than the half-life time of most unstable isotopes, and therefore the decay will likely not happen before another neutron is captured to form a new isotope. The capturing happens until the so-called neutron drip line is reached. When this happens, captured neutrons are immediately emitted from the core. Since capturing more neutrons is not possible any longer for the atom, the process temporarily ceases until β^- decay takes place. At this point, β^- decay, neutron-capture, and reaching the neutron drip line will directly follow one another in that order. That is, until the nucleus arrives at a “magic" atomic number. These magic numbers correspond to closed nucleon shells, and isotopes with these atomic numbers have a stable core. At this point, the quick series of neutron-capture can continue until the next neutron drip line.
The extreme conditions needed for the r-process usually are not maintained for long periods of time. After a series of neutron-captures, the neutron density drops. If the density is not large enough to continue the neutron-capture process, the isotope will, instead of capturing another neutron, repeat the decay in a series of beta decays until a stable isotope is formed.
The r-process has been speculated to take place in several different site, including magnetorotational supernovae (Tsujimoto & Nishimura, 2015) and collapsars (Siegel et al., 2019), though so far it has only been observed in NSMs (Rosswog et al., 2018). Therefore, this work will only consider NSMs as a site for the r-process.

2.6 Inflow and Onflow

As established before, galaxies accrete gas from the CGM for star formation to be sustained. The accretion of CGM gas, sometimes also referred to as onflow, will cause the abundance of metals in the disc to decrease. This is because the CGM largely consists primordial gas.
After being accreted, the angular momentum of the infalling gas drives radial flows, or inflow, within the galaxy. The CGM has a lower angular velocity and momentum than the disc gas. As the rotation curve of M33 is nearly flat (Corbelli, 2003), the angular momentum of the galaxy is larger at larger radii and decreases inwards. When the CGM gas falls into the disc, the infalling and pre-existing gasses mix. The total angular momentum of this mixture decreases with respect to the rest of the gas at the same radius. Conservation of angular momentum drives the mixed gas inwards until it reaches a point where the disc angular momentum is equal to the

angular momentum of the mixture. The accreted gas also drives metal-rich disc gas inwards, and therefore increases the metal abundance in the inner regions of the galaxy, while driving it out of the outer regions.

2.7 Outflow

The mixing of CGM gas with galactic gas does not only happen through accretion, but also in the CGM through outflowing galactic gas. One cause of outflow is related to star formation. That process heats some of the surrounding cool gas to the hot phase as well, which is partly ejected from the galaxy into the CGM.
When stars reach the end of their stellar life and release their gas in various events discussed above, part of the ejected gas is ejected from the galaxy .
The last case of outflow we will consider is a constant loss of hot gas, unrelated to stellar formation and death. Specially in smaller galaxies, like M33, the sound speed of the hot gas is on the order of the escape speed. It is therefore likely that smaller galaxies lose more of their hot gas.
All of the outflowing gas mixes with the metal-poor CGM gas. Although the CGM is no longer exactly primordial, the metallicity of the general CGM does not increase much due to its large size. When we do not take the CGM as one whole, we see that the CGM gas close to the disc can become slightly enriched by the effect of outflows.

3 The Model

To study the chemical evolution of M33, we use RAMICES II, developed by Fraser-Govil (2022). This model was based on the work of Schönrich & Binney (2009). RAMICES II simulates a disk galaxy over time, tracking the main events that impact the chemical composition of the galaxy. It is an axisymmetric model, in which a disc galaxy is decomposed in N rings with different radii R_i and width ΔR_i that together form a disc of radius R. In our case, we set it to 80 rings spanning a total radius of 15 kpc. The ring-based approach allows us to distinguish the features that belong to the center from those of the outer regions, and to study the evolution of radial profiles of relevant quantities.
For each ring, the model tracks stars that are living and the remnants of those that have undergone stellar death in a stellar reservoir. At every timestep (in our case $\Delta t = 0.01$Gyr), the model also recalculates the properties and metallicity of the gas reservoir, which differentiates hot ($\sim 10^7$K) and cold, star forming (~ 10K) gas. This continues for the entire duration of the simulation ($t = 10$Gyr, comparable to the current age of M33). The gas in this gas reservoir can have one of 3 origins: accreted, stellar, or remnant. Stellar gas comes from events that mark stellar death (ccSNe and AGB events) and remnant gas originates from SNIa and NSM. The accreted gas is CGM gas that enters the galaxy. The gas surrounding the galaxy in the CGM is contained in its own reservoir, which traces the metallicity. Although the CGM is known to be non-uniform, the model simplifies it to a single well-mixed reservoir, that reflects the average abundances, eliminating spatial dependence.
RAMICES II traces 12 elements: H, He, Fe, O, Mg, C, Si, Ca, Mn, Cr, Co and Eu. Below we describe how the model treats the chemical evolution.

3.1 Galactic Evolution

The model starts the simulation with baryonic mass M_0 that is significantly smaller than the current baryonic mass. All the gas that makes up the galaxy is primordial. The content of this gas can be found in Figure 1. Here, we find that hydrogen makes up approximately 75% of the simulated M33 and helium approximately 25%, constant over radius. There are some metals present in the primordial gas as well, but the total metallicity Z is so low ($\sim 10^{-8} - 10^{-9}$) that we can neglect it.
Over time, the baryonic mass of the simulation will increase to $M = 6.4 \times 10^9 M_\odot$ (Corbelli 2003; van der Marel et al. 2012), the observed mass of M33. This happens due to the accretion of CGM gas. We chose to model the accretion of gas exponentially over time. The accretion rate

$$\dot{\mathrm{M}} = \frac{\mathrm{M}_1}{b_1} e^{-t/b_1} \tag{5}$$

has a long timescale to sustain star formation. This is based on the exponential infall model in Schönrich & Binney (2009), but excludes the short timescale, which would guarantee an early peak for star formation. M_0, M_1, and b_1 are some of the parameters we try to constrain in this thesis.
The radial distribution of the accretion is not treated in Eq 5, but is determined separately, taking into account both radial infall and radial gas flows within the disc. We assume a linear relation between the rotational velocities of the galaxy v_c and the CGM

$$v_{\mathrm{CGM}}(R) = v_c \left(b + a \frac{R}{R_{\mathrm{out}}} \right) \tag{6}$$

where $R_{\mathrm{out}} = 15$kpc is the radius of M33. a and b are parameters to be determined in this work. b refers to the specific angular momentum of the CGM relative to galactic disc in the center

($R = 0$), while $a + b$ marks the relative angular momentum on the outer edge of the galaxy ($R = R_{\text{out}}$). Though there are no values associated with v_{CGM} and v_c in the model, there are important assumptions made that influence this relation. We assume the disc rotational velocity to be independent of radius. Another assumption we make is for the rotational velocity of the disc to be larger than the CGM, leading the sum of the parameters $a + b$ to be smaller than 1. The parameterization of this relation is used to derive the ratio between inflow and onflow for the ring at radius R_i,

$$B_i = \frac{\Delta M_{\text{inflow}}}{\Delta M_{\text{onflow}}} = \frac{2}{R_i \left(\Delta R_i + R_{i+1}\right)} \left(\frac{a}{4R_{\text{out}}} \left(R_{i+}^4 - R_{i-}^4\right) + \frac{(b-1)}{3} \left(R_{i+}^3 - R_{i-}^3\right) \right) \tag{7}$$

where $R_{i\pm} = R_i \pm \frac{\Delta R_i}{2}$ are the radii of the two neighbouring rings (Bilitewski & Schönrich, 2012). This ratio is used to calculate how much of the accreted gas comes from inflow or onflow, where onflow corresponds to gas accreted from the CGM and inflow is due to radial flows.
Starting at the innermost ring, the model computes the amount of mass that is expected, $M_{i,\text{new}}$. From there, it calculates how much mass has to be added to the ring in order to reach $M_{i,\text{new}}$. The reason why the gas mass is usually lower than $M_{i,\text{new}}$ is because the gas reservoir loses mass every timestep to star formation. The difference between the current mass and the new mass is ΔM. With the help of Eq 7 the model computes how much matter flows in, $\Delta M_{\text{inflow}} = \frac{B_i}{1+B_i} \Delta M$. This ΔM_{inflow} is subtracted from the mass of the next ring M_{i+1}. Infall from the CGM increases the mass of this ring until $M_{i,\text{new}}$ is reached, $\Delta M_{\text{onflow}} = \Delta M - \Delta M_{\text{inflow}}$. This process repeats for every ring, except for the outermost ring. The final ring does not gain mass from radial flows, so the entire mass required to reach M_{new} is directly accreted from the CGM, $\Delta M = \Delta M_{\text{onflow}}$, $\Delta M_{\text{inflow}} = 0$.
Other than accreting, the galaxy also ejects gas, specifically from the hot gas reservoir. The fraction of hot gas ejected at every timestep is encapsulated in the parameter $f_{\text{h, expelled}}$, the value of which will be determined in this thesis.

Infall plays a key role in shaping the galaxy and its radial structure. We chose to adopt an inside-out formationfrom the original model by Schönrich & McMillan (2017)). The scale length of the gas disc grows with time as

$$R_{\text{gas}}(t) = R_0 + \mathcal{N} \left(\arctan\left(\frac{t - t_0}{t_g}\right) - \arctan\left(\frac{t_0}{t_g}\right) \right) \tag{8}$$

with $\mathcal{N}$ as a normalization constant to ensure $R_{\text{gas}}(t_{\text{final}}) = R_{\text{final}}$. The parameters t_0, t_g, and R_0 will be varied to find a fiducial for the model. t_{final} and R_{final} are set at the current scale length and duration of the simulation, $t_{\text{final}} = 10\text{Gyr}$ and $R_{\text{final}} = 4.5\text{kpc}$. The gas scale length is an estimation based on the molecular and atomic hydrogen content of M33 (Gratier et al., 2010).

3.2 Stars

Figure 1 shows that over the course of the simulation, the overall helium and metal abundances increase. This is caused by stellar evolution, and this section will describe the works of this in the code.
In terms of this model, stars take gas out of the gas reservoir when they are being formed. This gas comes back into the gas reservoir through stellar death events, with a different abundance than before.

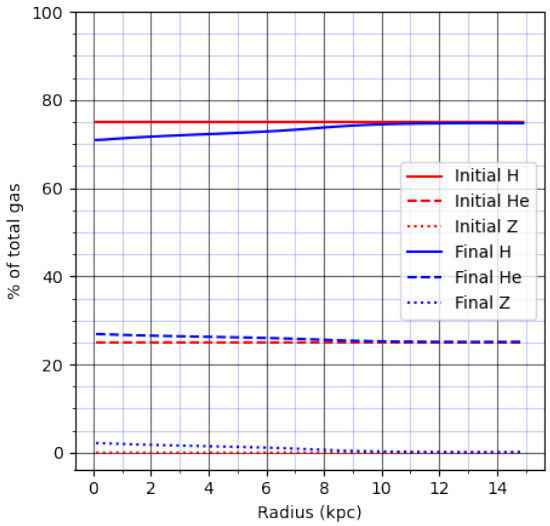

Figure 1: The content of the M33 simulation at $t = 0.00$ Gyr and $t = 10.00$ Gyr

Section 2.1 mentions that a modified version of the Schmidt-Kennicutt law applies to M33. The modification ensures that at low surface densities, stars are not able to form as easily:

$$\dot{\Sigma}_* = \begin{cases} \kappa \Sigma_{\text{gas}}^{n1} & \Sigma_{\text{cold}} > \Sigma_{\text{cut-off}} \\ \kappa \left(\Sigma_{\text{cut-off}} + \Sigma_{\text{hot}}\right)^{n1-n2} \Sigma_{\text{gas}}^{n2} & \text{otherwise} \end{cases} \tag{9}$$

Here, the surface density of the gas is split up into two surface densities, one for the hot gas reservoir Σ_{hot} and one for the cold gas reservoir Σ_{cold}. Slope $n1$ is the same as n in Eq 1, with a value of $n1 = 1.4$, and the cut-off slope has a value of $n2 = 4.0$. The low end cut-off density $\Sigma_{\text{cut-off}}$ is something to be determined in this thesis and the proportionality prefactor at $\kappa = \left(2.2 \times 10^3 M_\odot \text{pc}^{-2}\right)^{1-n1}$ Gyr^{-1}.
The mass of stars determines the abundance of the ejected gas at the end of their life. As mentioned in Section 2.1, the way new-born stars are distributed into mass bins is not precisely known. The IMF RAMICES II follows is the Chabrier (2003) IMF. This adheres to the Salpeter law, but has a modification on the low-mass end:

$$\zeta(M) = \begin{cases} c_1 M^{-1} \exp\left\{\left(-\frac{\log_{10}\left(\frac{M}{0.08}\right)^2}{2\times 0.69^2}\right)\right\} & \text{if } M < M_\odot \\ c_2 M^{-\alpha} & \text{otherwise} \end{cases} \tag{10}$$

where c_1 and c_2 are normalization constants, and $\alpha = 2.35$ as determined by Salpeter (1955). Now, we can compute how many stars are formed in the ith mass bin every timestep:

$$\text{d}N_i = \frac{\text{SFR}(t)\text{d}t}{\int_0^\infty M\zeta(M)\text{d}M} \int_{M_i}^{M_{i+1}} \zeta(M)\text{d}M \tag{11}$$

As the consequence of the formation of massive stars, some of the surrounding gas is heated, and most of the heated gas is ejected from the galaxy into the CGM. This is described by the parameters η, which represents the amount of solar masses heated per $1M_\odot$ of stars formed, and e_{eject}, which sets the fraction of η that is immediately ejected from the galaxy. This set of

parameters does is largely unconstrained, and instead, will be varied to find a fiducial model.

Some stars that are created live considerably longer than any simulation of a galaxy, and these stars do not get to feed their interiors back into the galactic gas. This is the reason why the model does not track stars with $M_* < 0.3M_\odot$ in individual mass bins, and instead treats them as immortal stars.

The RAMICES II model does not track every star and element created. As an alternative, it uses the yields by Maeder (1992) and Marigo (2001) for H, He and CNO of low-mass stars that result in an AGB event to estimate the abundances of the gas that is to be released. Even though the s-process is not taken into account by these yields, this will not have an effect on the output, as RAMICES II does not trace typical s-process elements.
The content of the gas ejected during ccSNe is determined by Maeder (1992), Chieffi & Limongi (2004), and Limongi & Chieffi (2008) yields.
Not all intermediate-mass stars go ccSNe, a small fraction goes ecSN instead. To model this, we say that all $8.5 - 10M_\odot$ stars have a probability $p_{\text{ecSN}} = 0.01$ to undergo the rare ecSN, while the rest of the stars in this mass region become ccSNe. The content of the ecSNe ejecta follows the Jones et al. (2019) yields.
The temperature of the ejected material is not tracked by the code either. To determine whether this gas belongs to the hot or cold gas reservoir, fractions of ejected gas that goes into the hot gas phase are set per event. The values of these fractions can be found in Table 1, and are chosen to be consistent with Schönrich & Weinberg (2019).
As described in Section 2.7, part of the gas ejected during events is immediately ejected from the galaxy. This process is encapsulated in ℓ, a parameter that describes the fraction of released material that is ejected from the galaxy into the CGM.

3.3 Remnants

Remnant events also influence the chemical composition of a galaxy. Where stellar death follows from star formation, that took gas from the galactic gas reservoirs, remnant events evolve from stellar remnants, which are formed during stellar death. Therefore, remnant events do not require taking gas from the galactic gas reservoir, they only feed back.
Both remnants events described in Section 2.4 involve binary systems. Modeling these events would involve resolving the binary systems and the associated mass transfer. RAMICES II does not do this, hence some assumptions are made. Out of all the remnants, all those in the appropriate mass range are candidates to undergo SNIa or NSM. This is a fraction c_X, where X refers to the type of event. All candidates are placed in a "waiting room", until a delay time τ_X has passed. During this time, the binary system will evolve. The inspiralling does not have a certain time set, as it can differ per system. Instead, there is a probabilistic decay ν_X that defines how many progenitors have completed the spiraling inward and will explode per Gyr, given as $(1 - \exp(-\nu_X t))$. The onset for the SNIa is modeled as a double exponential: 99% follow a long spiraling timescale, but 1% of candidates explodes quickly. The values we assumed for these parameters can be found in Table 2.

The abundance of SNIa gas is set by the W70 Iwamoto et al. (1999) yields. For NSM, we assume that 100% of their mass is converted into heavier elements produced in the r-process. There are no yields available for NSM, so we calibrate the output to the Solar [Eu/Fe] abundance. Just like with stellar death events, the released gas is divided into the hot and cold gas reservoirs

through the parameters in Table 1. Both events also eject part of their gas out of the galaxy, set by ℓ.

Feedback source	Fraction hot gas
AGB	0.35
ccSN	0.60
SNIa	0.99
NSM	0.80

Table 1: The fractions of ejected gas going into the hot gas phase per event

Parameters	Value SNIa	Value NSM
c	0.07	0.00015
τ	0.45 Gyr	0.02 Gyr
ν	1.5 Gyr (99%) 1.0 Gyr (1%)	0.3 Gyr

Table 2: Parameters that simply the modeling of SNIa and NSM and their values

4 Observational Data

We compare the abundance gradient of our model with observed chemical abundances in M33. It is essential to gather a sufficiently large and representative sample of abundance data in order to smooth out any inhomogeneities or irregularities in the regions of observation, such as spiral arms. We decided to include multiple data sets that span a wide radial range for different origins of the observations.

Oxygen
Oxygen is one of the elements that is most frequently available in observational datasets. The oxygen data can be divided into 3 sources: HII regions, planetary nebulae (PNe), and young massive stars.
HII regions surround young massive stars and contain elements created by previous generations of massive stars. These massive stars form oxygen, so the HII regions are expected to be rich in oxygen. We look at data sets obtained by Smith (1975), Kwitter & Aller (1981),Vilchez et al. (1988), Crockett et al. (2006), Magrini et al. (2007b), Esteban et al. (2009), Bresolin (2011), and Toribio San Cipriano et al. (2016). We also take a look at a more recent gradient derived by Rogers et al. (2022).
PNe, observed by Magrini et al. 2004, 2009, are a remnant of low-mass stars dying. Generally, the oxygen abundance in PNe is lower than in HII regions. While HII regions represent the abundance of the current ISM, PNe reflect the abundance of an older population. The young massive stars in HII regions release more oxygen than the low-mass stars that produced the PNe, further contributing to the lower oxygen abundance observed in PNe.
Unlike the first two categories, massive young are not a region, but these measurements look specifically at individual stars. The oxygen abundance in giant stars was observed by Monteverde et al. (1997), Urbaneja et al. (2005) and Beaulieu et al. (2006). These measurements include A, B supergiant stars and Cepheids.

Iron
Iron is mostly created in massive stars and released during ccSNe and SNIa, however, most dataset available measure the iron abundance in AGB and RGB stars (Kim et al. 2002; Tiede et al. 2004; Cioni 2009). These low-mass stars represent an older population, and will show a lower abundance than the general ISM, which is enriched by other chemical evolution events.

Not all of the abundances have an error associated with it in their original paper. We decided to put the error of these measurements at 0.2 dex.

5 Results

In order to constrain chemical evolutionary parameters of M33, several models with different values for the key parameters were analyzed. The fiducial model will be discussed in this section. The parameters of the fiducial model, obtained by trial-and-error, are briefly discussed in Section 5.1, before we dive into the analysis of this model. First, we look at some basic properties of this model in Section 5.2. These include the rates of star formation and chemical evolution events, as well as the mass of the model galaxy. Then, in Section 5.3, we compare the metallicity gradients of the model with the observational data available to us, which were introduced in Section 4. The metals we will discuss in this section are oxygen and iron. We will also look at the time evolution of these gradients.

5.1 Fiducial Parameters

Parameters that describe the global structure of M33, such as the baryonic mass and scale length have been discussed previously. Other parameters, that currently have unknown or uncertain values, have been tested in various runs of the RAMICES-II simulation code. The fiducial values for M33 are presented in Table 3.

Parameter	Meaning	Value
M_0	Initial gaseous mass of the galaxy	$1.5 \times 10^9 M_\odot$
M_1	Mass of the onfall, Eq 5	$12 \times 10^9 M_\odot$
b_1	Timescale of the onfall, Eq 5	8 Gyr
t_0	Delay time before start growth of the scale length	1.5 Gyr
t_g	Timescale of initial growth of the scale length	0.6 Gyr
R_0	Initial scale length of gas disc	1.5 kpc
a	The inflow 'Bilitewski a factor', Eq 6&7	0
b	The inflow 'Bilitewski b factor', Eq 6&7	0.66
$\Sigma_{\text{cut-off}}$	Low density Schmidt cut-off density, Eq 9	$4 M_\odot \text{pc}^{-2}$
η	Mass heated per solar mass created	0.45
e_{eject}	Fraction of η ejected to the CGM	0.7
$f_{\text{h,expelled}}$	Fraction of hot gas ejected per timestep	0.005
ℓ	Fraction of yields ejected	0.55

Table 3: The parameters used in RAMICES II to obtain the fiducial model

5.2 M33 properties

Before going into the chemical abundances and evolution thereof, it is important to look into the basics of the M33's disc evolution, which in turn influence the obtained chemical compositions.

5.2.1 Star formation rate

Figures 2 and 3 show the star formation rate of our fiducial model. Figure 2 looks at M33 as a whole and shows the mass of the stars formed per year. Figure 3 looks at specific rings, with radii of 0.3, 2.0, 4.8, and 7.6kpc and shows the stellar mass formed per year at that radius. As displayed in the graphs, star formation has two peaks: one initial peak caused by a strong star formation rate in the center of the galaxy and one peak at a later time, caused by a peak in star formation outside the central regions of the disc. This is in line with inside-out formation,

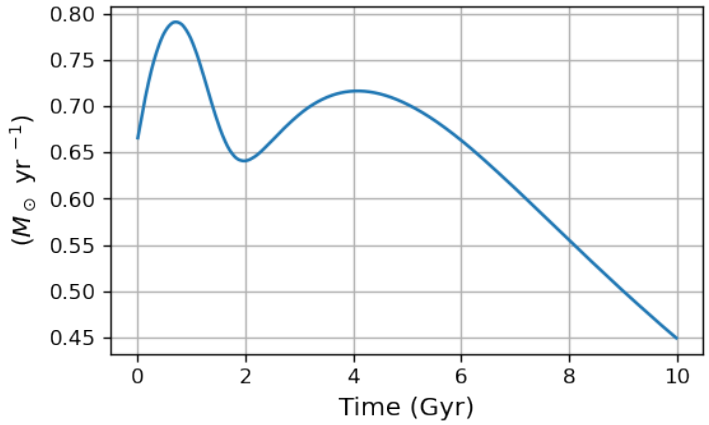

Figure 2: The mass of stars formed every year over the entire galaxy

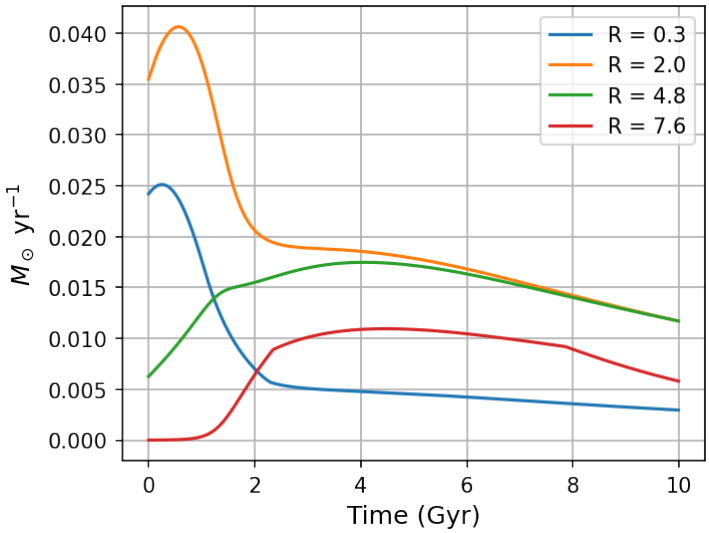

Figure 3: The stellar mass formed per year in the fiducial model at 0.3, 2.0, 4.8, and 7.6kpc

stating that the galaxy forms from the central regions outwards. The height of the second peak depends on the infall rate.
Magrini et al. (2007a) estimated a recent mean SFR $= 0.55 M_\odot \mathrm{yr}^{-1}$ $(1-4$ Gyr ago), and over a longer timescale $(1-8$ Gyr ago) the mean SFR increased to $1.1 M_\odot \mathrm{yr}^{-1}$. Using RAMICES II, the recent $(1-4$ Gyr ago) mean SFR we obtain is $\simeq 0.58 M_\odot \mathrm{yr}^{-1}$, in agreement with Magrini's findings. When looking at a broader history of M33, the model obtains a mean SFR $\simeq 0.65 M_\odot \mathrm{yr}^{-1}$. Figure 2 shows that the simulated M33 never reaches a SFR of $1.1 M_\odot \mathrm{yr}^{-1}$, not even during its star forming peak, where the model gives SFR$\simeq 0.79 M_\odot \mathrm{yr}^{-1}$.

5.2.2 Events rates

Not all chemical evolution events start taking place immediately after forming the galaxy. Among stellar feedback processes, only ccSNe operate swiftly enough to influence the surrounding ISM immediately. The rate of events per timestep are important in understanding the element abundances. Figure 4 shows the number of events that take place per timestep at the same radii we

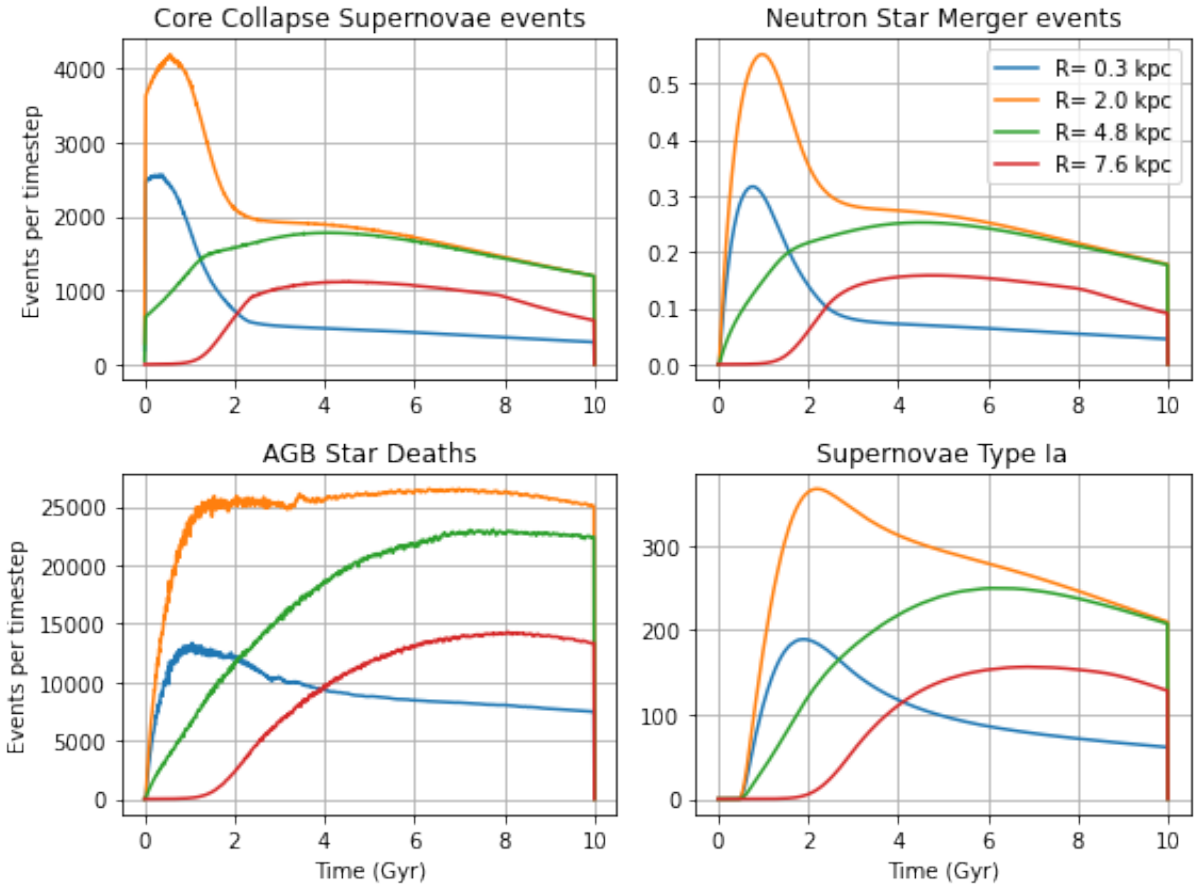

Figure 4: The number of events happening during each timestep of the simulation at 4 different radii. We look at ccSNe (**top left panel**), NSMs (**top right panel**), AGB deaths (**bottom left panel**), and SNIa (**bottom right panel**).

looked at before.

The top left panel of Figure 4, which shows the ccSNe rate, follows the same curves as the star formation rate in Figure 3. This is expected, as most of the stars that undergo ccSN were also created during the same timestep, or the previous one, due to their short lifetime.
The remnants for ccSNe are either neutron stars or black holes. A part of those neutron stars merge and create NSMs. As expected, the top right panel of Figure 4 shows that the rate of NSM events has a similar shape, but is a bit delayed due to longer timescales.
Most of the stars that are formed do not end in a ccSN. Instead, they are low-mass stars, whose stellar life ends in an AGB event. Comparing the star formation rate in Figure 3 and AGB event rate in the bottom right panel of Figure 4, we see that after the peak in star formation has passed, the AGB rate keeps increasing, due to the long lifetime of low-mass stars.
The death of these stars leaves white dwarfs, of which a fraction will end in an SNIa. Comparing The two bottom panels in Figure 4, showing the AGB and SNIa event rate, we see a similarity in event rate, but after a few Gyr, the SNIa rate keeps decreasing when the AGB rate is roughly constant. This is once again explained by the longer lifetime. The stars with lower masses will leave white dwarfs that also have lower masses. These white dwarfs will take a longer time to exceed the Chandrasekhar limit, if they even reach it at all, and therefore do not lead to a SNIa

during the duration of the simulation.

5.2.3 Mass distribution

Next, we take a look at the evolution of the baryonic mass. Instead of setting a parameter for the final mass of M33 we check that the value at the present time is in agreement with observations. In our simulation, the final mass is influenced by several parameters, related to infall and outflow of gas. The total baryonic mass is made up of stars and gas. From observations, we know that the stellar mass component of M33 is estimated to be $3.2 \pm 0.4 \times 10^9 M_\odot$ (van der Marel et al., 2012), and the total gas mass is $\sim 3.2 \times 10^9 M_\odot$ (Corbelli, 2003). There is no precise error given for the latter estimate, though there are uncertainties related to the measurement. We decided to add an uncertainty of 20%, which is equal to $0.64 \times 10^9 M_\odot$. Combining these masses, we obtain a total mass for M33 of $6.4 \pm 0.8 \times 10^9 M_\odot$. The total mass evolution of the simulated M33 can be found in Figure 5, together with the literature values for the masses, which are displayed as points at $t = 10$Gyr, the end time of our simulation. The final mass of the simulation is $6.1 \times 10^9 M_\odot$ with a stellar component of $3.2 \times 10^9 M_\odot$, in excellent agreement with the observational data.
Figure 6 shows the radial profile of the stellar surface density and the surface density of the gas disc at multiple times of the model. In the left panel, we identify a break in stellar surface density at $\sim$ 8kpc, after which the profile steepens. This is in agreement with the findings of Ferguson et al. (2007), who discovered a break in surface brightness profile of M33 at this same radius.

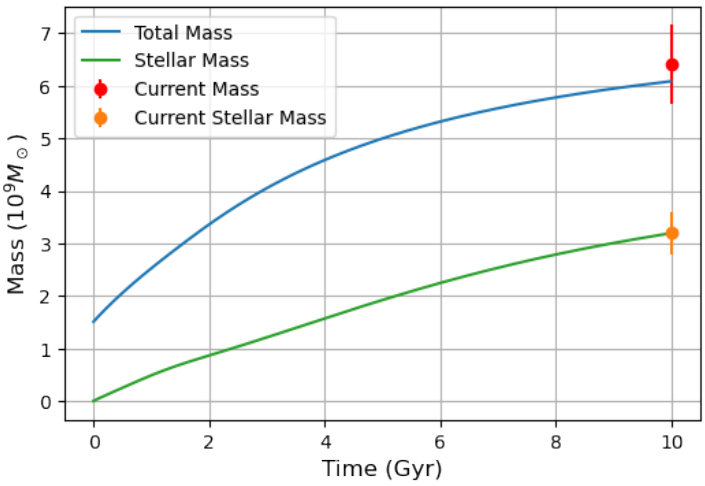

Figure 5: The time evolution of the total and stellar mass of the simulated M33, compared to the present-day observational estimates

5.3 Radial abundances and gradients

5.3.1 Oxygen

We show the oxygen abundances in the ISM, predicted by our fiducial model as a function of galactic radius in Figure 7. The radial oxygen abundance is pictured at 5 different times: 8 Gyr ago, 6 Gyr ago, 4 Gyr ago, 2 Gyr ago, and now. As we compare the model abundances to the

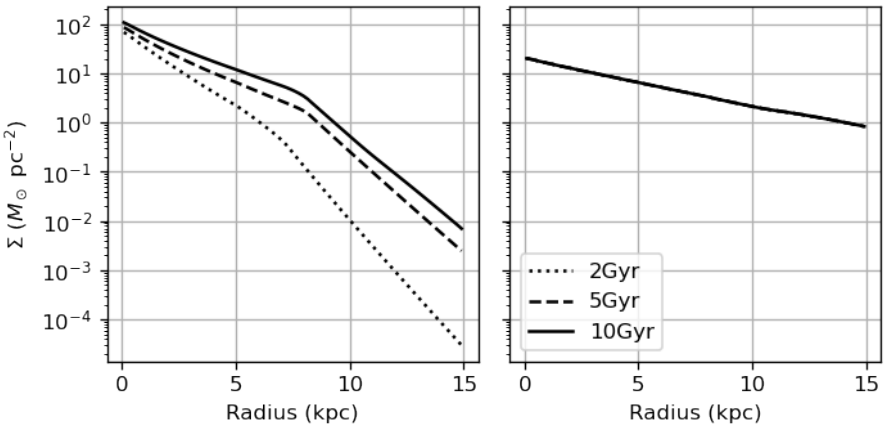

Figure 6: The stellar (**left panel**) and gas disc (**right panel**) surface density in the fiducial model at 2, 5, and 10 Gyr.

	Present $t = 10$Gyr	2 Gyr ago $t = 8$ Gyr	4 Gyr ago $t = 6$ Gyr	6 Gyr ago $t = 4$Gyr	8 Gyr ago $t = 2$ Gyr
O/H	-0.035 ± 0.001	-0.037 ± 0.001	-0.046 ± 0.001	-0.075 ± 0.001	-0.154 ± 0.005
Fe/H	-0.056 ± 0.001	-0.063 ± 0.001	-0.080 ± 0.001	-0.119 ± 0.001	-0.187 ± 0.005

Table 4: The linear fit gradients obtained by the model for the central 7 kpc at different times in units dex kpc^{-1}.

observed ones from HII regions, giant stars, and PNe, it is critical that we do not only look at the present-day trend, but also earlier ones, as not all of the observed abundances represent the present-day gas composition. We notice that the sharp decrease in oxygen coincides with the observed break in the stellar surface brightness at $\sim$ 8kpc.
We performed a linear fit on these curves, and the obtained gradients can be found in Table 4. The fit was performed for the inner 7kpc, where the gradient is approximately linear. Most observational data points also lie within this radius.
In a previous chemical evolution model by Magrini et al. (2007a), an oxygen gradient at present-time of -0.067 dex kpc^{-1} from 1 to 10 kpc was obtained. This is notably steeper than gradients we found using RAMICES II. The reason why they were able to find a gradient up until 10 kpc, is because they did not include the Kennicutt-Schmidt surface density cut-off (Eq 9) in their model.

The top panel in Figure 7 compares the predicted radial oxygen abundance to abundances measured in HII regions. A linear fit through all the data points in this panel gives an oxygen gradient of -0.052 ± 0.033 dex kpc^{-1}. The gradient here is similar to the gradient of our fiducial model. Even closer is our model to the more recently derived gradient of -0.037 ± 0.0007 dex kpc^{-1} (Rogers et al., 2022). We see that most data points in Figure 7 lie a few tenths of a dex lower than our model. This can be explained by the calibration differences, systematically shifting entire datasets by a few tenths of dex. This problem also affects comparisons between observational datasets that were derived using different techniques and abundance tracers (Sanders et al., 2017).

The middle panel of Figure 7 displays the oxygen abundance of several PNe, compared to the predictions of our model. A linear fit through the data points of the PNe gives a gradient of -0.037 ± 0.043 dex kpc^{-1}(Magrini et al. 2004, 2009). As explained in Section 4, we do not ex-

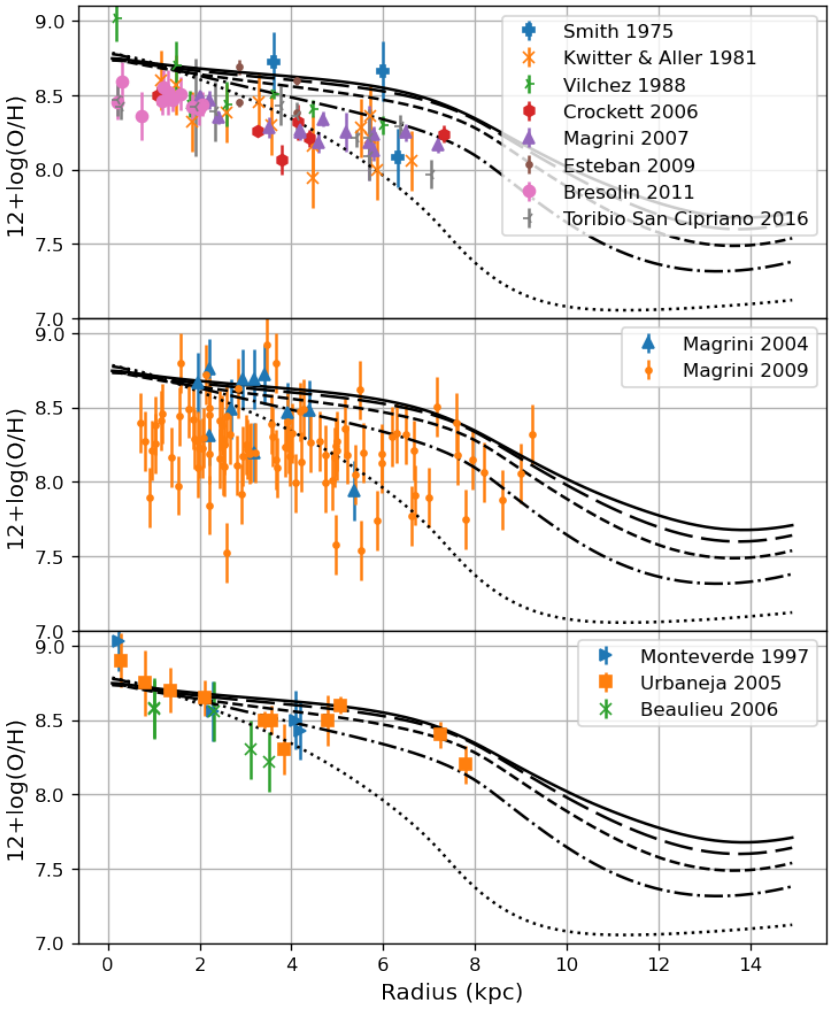

Figure 7: The radial gas phase oxygen abundance in our fiducial model as a function of radius compared with the oxygen abundances observed in HII regions (**top panel**), PNe (**middle panel**), and young massive stars (**bottom panel**) in M33, at times 2 Gyr (*dotted*), 4 Gyr (*dot-dashed*), 6 Gyr (*dashed*), 8 Gyr (*long dashed*), and 10 Gyr (*solid*).

pect the PNe data to follow the present-day oxygen curve, but instead some earlier curve. The observed PNe are $1 - 8$Gyr old, however we do not know the age of individual PNe. The mix in ages, which we cannot disentangle, implies that we cannot separate the different gradients in the total gradient of -0.037 ± 0.043 dex kpc^{-1}, and therefore trace the evolution of the oxygen abundance in the ISM in earlier times. In general, due to the inside-out formation of the galaxy, we expect that older stars are located at the center of the galaxy, and outskirt regions mostly consist of newer stars. Older stars form metal-poor PNe, while the newer stars form PNe with a higher oxygen abundance, as the ISM surrounding them was enriched before star formation. Therefore, we believe the data points in the center may follow an ealier abundance curve than the points further out.
It is also important to note that the observed location of a PN can be influenced by radial migration, meaning that the current radius of the PN can be different than its birthplace. Observations of an abundance gradient could indicate whether the radial migration was effective. When a metallicity gradient survives, the radial migration that took place in the galaxy is limited.

The linear fit through the data points (-0.037 ± 0.043 dex kpc^{-1}) indicates that the observed gradient is compatible with zero, i.e. a flat abundance profile. It is therefore possible that radial migration has contributed to this, and PNe have migrated both inward and outward, but as we only model gas and no stellar abundances we cannot confirm this.. If that is the case, our model cannot reproduce the observed gradient.
Overall we see that the gradient of the observed PNe is flatter than any of our model curves. This is reasonable, taking into account the effects of radial migration and radial age gradient due to inside-out formation.

In the bottom panel of Figure 7, the radial oxygen abundance at different times are compared to the abundances measured in young massive stars and Cepheids. By fitting a linear model to the data points, we determined a gradient of -0.11 ± 0.02 dex kpc^{-1}. The observational abundances in young stars by Urbaneja et al. (2005) seem to agree with the present-day oxygen abundance of our fiducial model. The gradient from this dataset alone is -0.052 ± 0.017 dex kpc^{-1}. The other two data sets have significantly steeper gradient (both -0.13 ± 0.04 dex kpc^{-1} (Monteverde et al. 1997; Beaulieu et al. 2006), possibly due to the small number of data points.

5.3.2 Iron

Figure 8 shows the radial iron abundance as predicted by our fiducial model for M33 at 5 different times compared to the observed abundances in low-mass stars of older populations. The linear fit gradients for all 5 curves can be found in Table 4. Radial migration plays a role here too, but considering that the gradient survives, the migration is likely limited. As with the oxygen in PNe, we expect the RGB and AGB stars to follow a negative age gradient: the oldest stars are located at lower radii. By looking at the model curves, we except the observed gradient to be flatter than the gradients $2 - 8$ Gyr ago.
The observational data points derived by Kim et al. (2002) have a gradient of -0.4 ± 0.02 dex kpc^{-1}, though crowding in the innermost points is severe. Excluding those, they find a gradient of -0.08 ± 0.03 dex kpc^{-1}. With this same strategy, Tiede et al. (2004) found an iron gradient of -0.07 ± 0.1 dex kpc^{-1}. As expected, these are flatter than the gradients predicted by our model at earlier times. A gradient of -0.078 ± 0.003 dex kpc^{-1} derived by Cioni (2009) also follows this trend.

5.3.3 Oxygen-Iron evolution

Now that we have established that our fiducial model produces oxygen and iron abundance gradients similar to the observed ones, we can take a look at its evolution. Figure 9 shows the relation between the [O/Fe] and [Fe/H] ratios. It is shown for all 80 ring radii of the model, where blue corresponds to the central regions of the galaxy and red curves represent the outskirts. In Section 5.3.1, we used $12 + \log\left(\frac{\mathrm{O}}{\mathrm{H}}\right)$, based on the ratio of number densities, as a measurement for the oxygen abundance, but here we converted this to [O/H], defined as

$$[\mathrm{O/H}] = \log\left(\frac{N_{\mathrm{O}}}{N_{\mathrm{H}}}\right) - \log\left(\frac{N_{\mathrm{O},\odot}}{N_{\mathrm{H},\odot}}\right) \tag{12}$$

so that it is normalized to the Sun. In Eq 12, N_{O} and N_{H} represent the number densities of oxygen and hydrogen in the ISM, and $N_{\mathrm{O},\odot}$ and $N_{\mathrm{H},\odot}$ represent the number densities of oxygen and hydrogen in the Sun (Magg et al., 2022). The [O/Fe] ratio is obtained by subtracting the individual ratios, [O/H]−[Fe/H].
We notice that, at low [Fe/H], the [O/Fe] ratio tends to be constant. Beyond a certain metallicity,

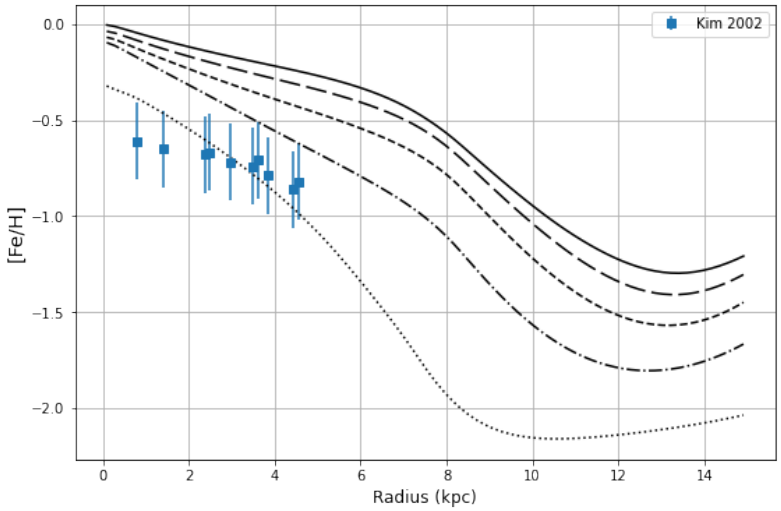

Figure 8: The radial gas phase iron abundance in our fiducial model as a function of radius compared with the iron abundances observed in RGB stars. The plot has the same line types as in Figure 7.

a decrease happens, the location of which changes with the radius. The “knee" in this [O/Fe] ratio happens when Type Ia SNe start taking off, which we can also see in the bottom right panel in Figure 4. Before the onset of SNIa, ccSNe are the only event to produce iron. Most oxygen is also released during ccSNe. The ratio between oxygen and iron ejected into the ISM by ccSNe is roughly constant. SNIa convert nearly all the available oxygen in their core into iron. The gas they release is therefore rich in iron but very poor in oxygen. This causes the [O/Fe] ratio to decrease at large iron abundance. There are currently no observational datasets available to test our models ability to predict the relation between the [O/Fe] and [Fe/H] ratios.

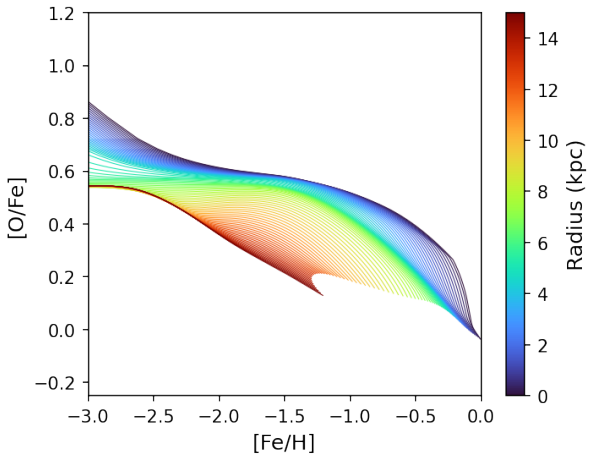

Figure 9: The time evolution of the relation between oxygen and iron abundance in the ISM predicted by our fiducial model

6 Discussion

In order to support our evolutionary choices in RAMICES II and see their influence on the predicted abundances and gradients in M33, we modify some of the assumptions we made in the fiducial model and inspect the outcomes of these new models. We consider models without radial flows, without inside-out growth, and without a low-density cut in the star formation law. We present the results in Section 6.1. To support our choice of value for the radial flow parameters in the fiducial model, we explore the effect of these in Section 6.2. Finally, we take a look at some sources of error and recommendations for improvement when it comes to the chemical evolution of M33 in Section 6.3.

6.1 Exploring the effect of different assumptions

In order to test the validity of our evolution choices, we decided to see what the model produces if we neglect some assumptions. For this, we decided to focus the radial oxygen abundance, as this is the elements with most observational data available to us. For illustration purposes, we decided to exclude a few datasets that either had unreliable or overabundant points, some that did not specifically state errors, or those sets that did not add any information visually. We made sure to include at least one dataset per source (HII, PNe, young massive stars) in the plots. The abundances of HII regions are red, PNe are green, and young massive stars are blue.
Figure 10 shows the radial oxygen abundance for different scenarios for galactic evolution. In the top left panel we see the fiducial model, the same as in Figure 7. In the middle left panel, we see how the radial oxygen abundance would evolve if M33 did not form from the inside-out, and the scale length stayed constant in time.The bottom left panel combines the absence of inside-out formation with an absence of radial flows and plots the radial oxygen abundance of M33 if the scale length stayed constant in time and there were no radial flows. In the middle right panel we see what the radial oxygen abundance would look like if there was no low density cut-off in the Kennicutt-Schmidt law. The bottom right panel shows the radial oxygen abundance for a model without radial flows. The gradients for all models can be found in Table 5.

The middle right panel in Figure 10 shows that the break in oxygen at $\sim$ 8kpc is caused by the inclusion of the cut-off density in the Kennicutt-Schmidt law. This is expected, as this cut-off causes less star formation in the outskirts of the disc, and in turn less metal production, to take place there.

In the bottom panels, showing the oxygen gradient for the models without radial flows, we see that the predicted present-day oxygen gradient is approximately flat until the break. Radial flows clearly drive a negative metallicity gradient in M33 and in galaxies in general. As star formation takes gas out of the ISM more gas needs to be accreted to sustain this. Without radial flows, all the new gas is accreted directly from the CGM. In contrast, radial flows supply gas with a higher metallicity than the CGM to the central regions, due to the mixing of infalling and disc gasses at the larger radii. At radii closer to 8kpc radial flows therefore remove metal rich gas and transport it to the center, which also necessitates more accretion of metal poor gas from the CGM or even higher radii. In the models without radial flows, such inward transport does not occur, and there is less need for accretion gas that will dilute the metal abundance in the interstellar medium. The middle and bottom panels on the left in Figure 10 show that radial flows are very influential on the metallicity gradient.

If the scale length of M33 was constant throughout time, this would barely be noticeable in

(*1*)	Present $t = 10$Gyr	2 Gyr ago $t = 8$ Gyr	4 Gyr ago $t = 6$ Gyr	6 Gyr ago $t = 4$Gyr	8 Gyr ago $t = 2$ Gyr
Middle left	-0.025 ± 0.002	-0.025 ± 0.002	-0.026 ± 0.002	-0.031 ± 0.002	-0.040 ± 0.002
Middle right	-0.026 ± 0.001	-0.30 ± 0.001	-0.040 ± 0.001	-0.69 ± 0.001	-0.127 ± 0.002
Bottom left	0.0001 ± 0.0002	-0.001 ± 0.0001	-0.004 ± 0.0001	-0.010 ± 0.001	-0.022 ± 0.001
Bottom right	-0.008 ± 0.002	-0.011 ± 0.002	-0.020 ± 0.002	-0.049 ± 0.001	-0.131 ± 0.003

Table 5: The linear fit oxygen gradients of models following different assumptions for the central 7 kpc. Column (*1*) represents the panel in Figure 10 and therefore model choice that the gradients are associated with.

the present-day oxygen gradient. The influence of the inside-out formation is only recognizable in past gradients. Closer to the formation time of M33 ($\sim 6 - 10$ Gyr ago), the influence of inside-out formation is the most significant, and the lack of a radial age gradient produces a flat metallicity gradient from an earlier age, in line with our expectations. Hence, the only way we can try to draw a conclusion about the presence of the inside-out formation in M33 is by using an older population such as PNe data (green points) compared to the older oxygen curves in the middle left panel and Table 5.

The gradient of the PNe datasets is -0.037 ± 0.043 dex kpc^{-1} (Magrini et al. 2004, 2009), and we expect the observed gradient to be flatter than the model gradients, as explained in Section 5.3.1. As this effect on the stellar gradient is at least in parts also dependent on the presence of inside-out formation, and the data has quite a larger error, the gas phase oxygen gradient in our models cannot provide evidence for or against the role of inside-out formation in the formation of M33.

Therefore, we take a look at the iron gradient and observed abundances in RGB stars (Kim et al., 2002) in Figure 11 to see whether they show a stronger dependence of inside out formation. Again, we expect a radially decreasing average stellar age (from inside-out formation) to flatten any gradient observed in stars: The RGB stars in Kim et al. (2002) have an age between 5 and 8 Gyr, meaning that the observed radial iron abundance would combine the two blue lines in the top two panels (8 and 6 Gyrs ago) of Figure 11, following the younger population more closely in the outskirts. This produces an observed stellar gradient flatter than the gas phase gradient of either age. On the other hand, we see that a model without inside-out formation also produces a flattened iron gradient in the ISM, the difference decreasing with time. Therefore, and with the added complication of radial migration, generally flattening stellar abundance gradient, based on these gradients alone, we cannot draw conclusion on whether inside-out formation took place in M33. Research has been done on M33 before, to figure out the evolution of its scale length. Williams et al. (2009) showed observational support for inside-out growth in M33 using photometry to show an average stellar age gradient. Based on this, we can conclude that the fiducial model that includes this evolution of the scale length is likely a more accurate description of M33 than a model with a constant scale length.

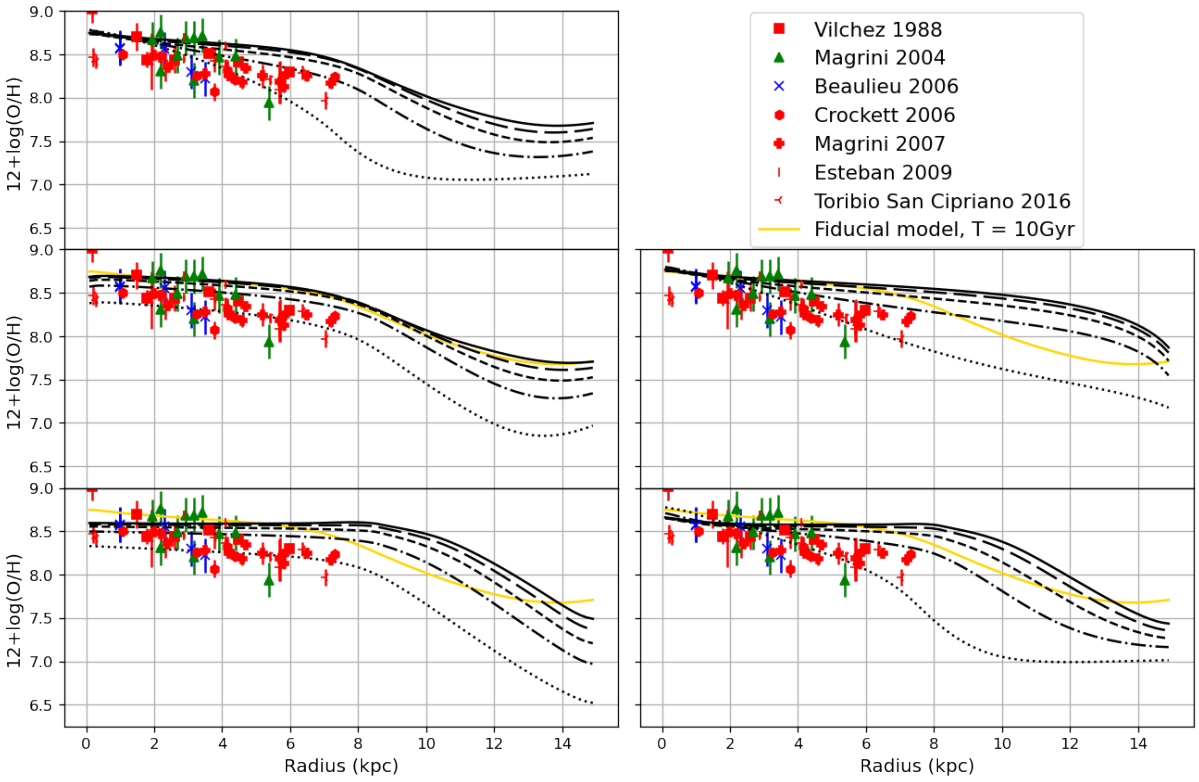

Figure 10: The radial oxygen abundance for models with different assumptions. Shown are the fiducial model (**top left panel**), a model without inside-out formation (**middle left panel**), a model without inside-out formation and radial flows (**bottom left panel**), a model without a low density cut in star formation (**middle right panel**) and a model without radial flows (**bottom right panel**). The line types are the same as in Figure 7.

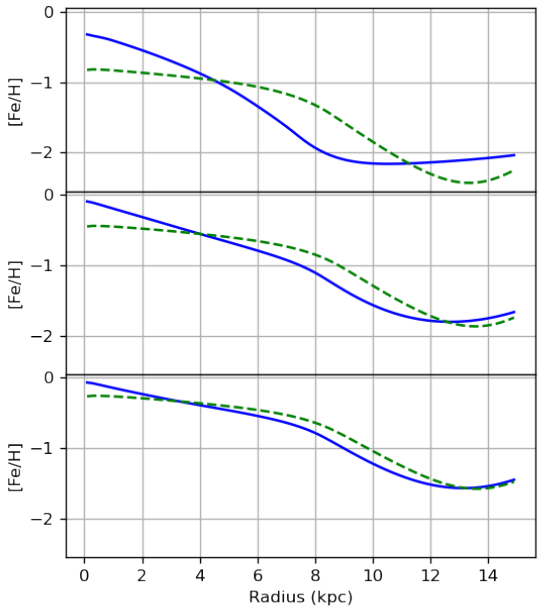

Figure 11: The radial iron abundance in M33 predicted by models with inside-out formation (*blue solid line*) and constant scale length (*green dashed line*) at 2 Gyr (**top panel**), 4 Gyr (**middle panel**) and 6 Gyr after formation (**bottom panel**)

6.2 Exploring the effect of different inflow parameters

Now that we have established that radial flows are very influential on the metallicity gradient and they are likely to take place in M33, based on the modeled and observed abundances, we can vary the parameters guiding the angular momentum mismatch between the CGM and the disc as in Eq 6. The effect of the radial flows increases with time, therefore we will look at the present-day gradient. Radial flows affect oxygen and iron to the same extend in this model. Analyzing models with different radial flows will therefore only be done to one of the abundances analyzed before. The element of our pick here is oxygen. Figure 12 shows the present-day radial oxygen abundance for models with different inflow parameters. In the Figure 12, 7 different curves are plotted, yet only 5 are visible. The yellow curve ($a = 0.66$, $b = 0$) is directly underneath the red curve ($a = 0.2$, $b = 0.2$), and the green curve ($a = 0.5$, $b = 0.5$) is covered in its entirety by the brown curve ($a = 0$, $b = 1$). The differences in prediction beyond $R \sim 7$kpc will not be analyzed, as there are no data available in this region, therefore we cannot draw conclusions.
The parameterization for the rotational velocity has a constant and a radial term. We notice that models where b, the constant term in Eq 6, dominates, the produced metallicity gradient are flatter than models with a dominant a, radial term. Comparing our models to observations, the models with a low a value match the data better.

6.3 Caveats

The method of trial-and-error, used to derive the fiducial model, induces errors and uncertainties in the obtained parameters. Out of the 13 free parameters, we have looked into the effect of only 2 parameters (a & b) in Section 6.2. Here, we found that, though the presence of radial

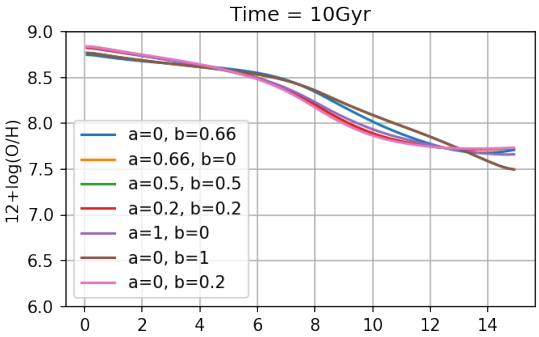

Figure 12: The present-day radial oxygen abundance predicted by the model for different values of the inflow parameters a & b. The green curve is overlapped by the brown curve, and the yellow curve is underneath the red curve.

flows have a significant effect on the metallicity gradient, the value for the inflow parameters does not. When the rotational velocity of the CGM is dominated by the radial term in Eq 6, we obtain steeper gradients than for models with the radius-independent term that dominates the CGM rotational velocity. In order to simplify the model, a value of $a = 0$ was chosen for the fiducial model, meaning that there is a constant mismatch between the rotational velocity of the disc and CGM. It could be true that the CGM rotational velocity is not flat. This is one of the uncertainties associated with the rotational velocity of the CGM, due to the difficulty of observations (Bregman et al., 2018).
Changing other parameters to have a significant effect on the metallicity gradients, causes other properties to differ from observations. Different M_0, M_1, and b_1 produces a total baryonic mass that deviates from the observed mass, therefore making us believe that the values in the fiducial model are relatively well-chosen. The ejection parameters η, e_{eject}, $f_{\text{h, expelled}}$ and ℓ also influence the final baryonic mass of the model. Different combination of the mass and ejection parameters can produce an accurate total baryonic mass, but would yield a stellar mass that deviates from observations. A different $\Sigma_{\text{cut-off}}$ changes the position of the break in surface density, no longer in agreement with the findings of Ferguson et al. (2007), wo identified a break in surface brightness at $\sim$ 8kpc. Changing the scale length parameters t_0, t_g, and R_0 only significantly effects the metallicity gradients in the first 6 Gyr after formation. The available data that look at the abundance of older populations do not help us draw any conclusions about inside-out formation, as discussed before, but these parameters could be looked into more carefully in future works.

One other source of error in the model that has not been covered yet is the gas scale length R_{final}. This quantity combines molecular and atomic hydrogen. The scale length of molecular hydrogen was found to be $R_{\text{H}_2} = 1.9 \pm 0.1$kpc, however, the atomic hydrogen scale length could not be found, as the surface density stays nearly constant (Gratier et al., 2010). The value taken as $R_{\text{final}} = 4.5$kpc was an estimation based on these observations, but cannot be taken as a true literature value. The results of the fiducial fit could be improved by taking R_{final} as a fourteenth free parameter. An alternative possibility is to create a chemical evolution model that uses the stellar scale length instead of the gas disc scale length, as done by Marcon-Uchida et al. (2010). This would reduce uncertainties as the stellar scale length is better constrained.
Another observation that this model fails to include lies in the stellar disc. Robles-Valdez et al. (2012) finds that, while the gas disc indeed follows the inside-out formation, stars follow an inside-out formation only until $\sim$ 6kpc. For $R >$ 6kpc, stars seem to follow an outside-in for-

mation. This was not modeled by our simulation, and due to the limited observational data in stars at these larger radii, it was not identified in our analysis of the metallicity gradients.

In this work, we analyze the oxygen and iron gradients. Together, these elements cover most of the events that impact chemical evolution. However, with the absence of Europium in our analysis, we fail to examine the heavy element abundance in M33. By reviewing the model outcome and evaluating this against observed abundances of Europium, we can determine whether the Solar [Eu/Fe] abundance holds up in M33, and if there are other factors, not taken into account, at play that might influence the concentration of heavy elements. The reason why this analysis was not carried out is because the observed Europium abundances in M33 are limited (Larsen et al., 2022).

7 Conclusions

In this thesis, we have built a chemical evolution model with the aim to reproduce the observational data of the nearby disc galaxy M33 including baryonic mass, star formation rate, and metallicity gradients. We used the chemical evolution code RAMICES II and constrained our models with abundance measurements coming from a variety of tracers including HII regions, massive stars and planetary nebulae. Here, we present our findings:

i. Our fiducial chemical evolution model, which includes inside-out formation, a low surface density cut-off in the star formation low, and angular momentum-driven radial flows due to accretion of a slow-rotating CGM, produces radial abundances for oxygen and iron in agreement with the observational data.

ii. Our model produces a present-day oxygen gradient (for $R < 7$kpc) of -0.035 ± 0.001 dex kpc^{-1} of similar value to the observed gradient in HII regions by Rogers et al. (2022), who found a gradient of -0.037 ± 0.0007. The oxygen gradient predicted by the model is also in agreement with that observed in young massive stars (-0.052 ± 0.017 dex kpc^{-1},Urbaneja et al. 2005).

iii. The model was not able to predict a radial oxygen abundance similar to the observed abundances in planetary nebulae, possibly due to strong radial migration.

iv. The fiducial model predicts a present-day gradient for iron of -0.056 ± 0.001 dex kpc^{-1}, which is flatter than the observed abundances in RGB and AGB stars (-0.07 - -0.08 dex kpc^{-1}, Kim et al. 2002; Tiede et al. 2004; Cioni 2009).

v. Our model predicts a flattening of the gradient with time, which is in agreement with the observed abundance for iron in RGB and AGB stars, and could be in agreement with the observed abundances in PNe, if radial migration was relatively mild.

vi. The influence of the scale length evolution on radial metallicity abundances is negligible in the present-day. The effect of inside-out formation on the radial abundances was more pronounced at earlier times ($\sim 6-10$ Gyr ago), though based on the oxygen and iron abundances in older populations alone, we could not conclude whether the inside-out formation has taken place in M33 or not.

vii. The presence of radial flows driven by the conservation of angular momentum, following the accretion of gas from the CGM, has a significant influence on the metallicity gradients. We conclude that the observed gradients are best reproduced by a model that takes a constant rotational velocity in the CGM, equal to approximately $\frac{2}{3}v_c$, the disc rotational velocity.

viii. The observed break in surface density at $\sim$ 8kpc can best be modeled as a low surface density cut-off in the Schmidt-Kennicutt star formation law at $4M_{\odot}$pc^{-2}.

ix. The outflow of the model is mimicked by 3 processes of hot gas ejection, associated with star formation, stellar death events, and a constant loss. The fiducial model suggests that outflow plays a large role in M33.

x. In combination with the strong gas outflow, the exponential infall rate of the model produces total baryonic mass and stellar mass that are in good agreement with the observational data when the infall mass is roughly $12M_{\odot}$

8 Acknowledgments

This thesis would not have been possible without the support of many individuals. I would like to thank my supervisors Filippo and Jenny for their guidance throughout these busy weeks. They helped me understand many new aspects of chemical evolution and astronomy in general that I was unfamiliar with before the start of this project. I also want to express my gratitude for my friends in this study programme, who created such an encouraging and supportive environment in Kapteyn during this period.
Next to that, I would like to acknowledge my use of AI, specifically ChatGPT, which helped me scout for sources at the beginning of this journey, and formulate several individual sentences in this thesis, along with the Overleaf AI tool, which pointed out when my sentences were not grammatically.

References

Beaulieu J. P., Buchler J. R., Marquette J. B., Hartman J. D., Schwarzenberg-Czerny A., 2006, The Astrophysical Journal Letters, 653, L101

Bethe H. A., 1939, Phys. Rev., 55, 434

Bilitewski T., Schönrich R., 2012, Monthly Royal Notices of the Royal Astronomical Society, 426, 2266

Bregman J. N., Anderson M. E., Miller M. J., Hodges-Kluck E., Dai X., Li J.-T., Li Y., Qu Z., 2018, The Astrophysical Journal, 862, 3

Bresolin F., 2011, The Astrophysical Journal, 730, 129

Burbidge E. M., Burbidge G. R., Fowler W. A., Hoyle F., 1957, Reviews of Modern Physics, 29, 547

Chabrier G., 2003, The Publications of the Astronomical Society of the Pacific, 115, 763

Chandrasekhar S., 1931, The Astrophysical Journal, 74, 81

Chieffi A., Limongi M., 2004, The Astrophysical Journal, 608, 405

Cioni M. R. L., 2009, Astronomy and Astrophysics, 506, 1137

Corbelli E., 2003, Monthly Royal Notices of the Royal Astronomical Society, 342, 199

Crockett N. R., Garnett D. R., Massey P., Jacoby G., 2006, The Astrophysical Journal, 637, 741

Côté B., et al., 2019, The Astrophysical Journal, 875, 106

Diaz A. I., Tosi M., 1984, Monthly Royal Notices of the Royal Astronomical Society, 208, 365

Eddington A. S., 1920, The Observatory, 43, 341

Esteban C., Bresolin F., Peimbert M., García-Rojas J., Peimbert A., Mesa-Delgado A., 2009, The Astrophysical Journal, 700, 654

Ferguson A., Irwin2 M., Chapman S., Ibata R., Lewis G., Tanvir N., 2007, in DE JONG R. S., ed., Astrophysics and Space Science Proceedings Vol. 3, Island Universes. p. 239, doi:10.1007/978-1-4020-5573-7_39

Ferrini F., Poggianti B. M., 1993, The Astrophysical Journal, 410, 44

Fraser-Govil J., 2022, PhD Thesis, University of Oxford

Freedman W. L., Wilson C. D., Madore B. F., 1991, The Astrophysical Journal, 372, 455

Friske J. K. S., 2024, PhD Thesis, University College London

Gratier P., et al., 2010, Astronomy and Astrophysics, 522, A3

Hodges-Kluck E. J., Miller M. J., Bregman J. N., 2016, The Astrophysical Journal, 822, 21

Hoyle F., 1946, Monthly Royal Notices of the Royal Astronomical Society, 106, 343

Hoyle F., 1954, The Astrophysical Journal Supplement, 1, 121

Iwamoto K., Brachwitz F., Nomoto K., Kishimoto N., Umeda H., Hix W. R., Thielemann F.-K., 1999, The Astrophysical Journal Supplement, 125, 439

Jones S., et al., 2019, Astronomy and Astrophysics, 622, A74

Kam Z. S., Carignan C., Chemin L., Amram P., Epinat B., 2015, Monthly Royal Notices of the Royal Astronomical Society, 449, 4048

Kang X., Chang R., Yin J., Hou J., Zhang F., Zhang Y., Han Z., 2012, Monthly Royal Notices of the Royal Astronomical Society, 426, 1455

Kang X., Kudritzki R.-P., Zhang F., 2023, Astronomy and Astrophysics, 679, A83

Kennicutt Jr. R. C., 1998, The Astrophysical Journal, 498, 541

Kim M., Kim E., Lee M. G., Sarajedini A., Geisler D., 2002, The Astronomical Journal, 123, 244

Kroupa P., 2001, Monthly Royal Notices of the Royal Astronomical Society, 322, 231

Kwitter K. B., Aller L. H., 1981, Monthly Royal Notices of the Royal Astronomical Society, 195, 939

Larsen S. S., Eitner P., Magg E., Bergemann M., Moltzer C. A. S., Brodie J. P., Romanowsky A. J., Strader J., 2022, Astronomy and Astrophysics, 660, A88

Larson R. B., Tinsley B. M., Caldwell C. N., 1980, The Astrophysical Journal, 237, 692

Limongi M., Chieffi A., 2008, Online Repository for the Franec Evolutionary Output

Ma J., Zhou X., Chen J., Wu H., Jiang Z., Xue S., Zhu J., 2002, The Astronomical Journal, 123, 3141

Maeder A., 1992, Astronomy and Astrophysics, 264, 105

Magg E., et al., 2022, Astronomy and Astrophysics, 661, A140

Magrini L., Perinotto M., Mampaso A., Corradi R. L. M., 2004, Astronomy and Astrophysics, 426, 779

Magrini L., Corbelli E., Galli D., 2007a, Astronomy and Astrophysics, 470, 843

Magrini L., Vílchez J. M., Mampaso A., Corradi R. L. M., Leisy P., 2007b, Astronomy and Astrophysics, 470, 865

Magrini L., Stanghellini L., Villaver E., 2009, The Astrophysical Journal, 696, 729

Marcon-Uchida M. M., Matteucci F., Costa R. D. D., 2010, Astronomy and Astrophysics, 520, A35

Marigo P., 2001, Astronomy and Astrophysics, 370, 194

Mayor M., Vigroux L., 1981, Astronomy and Astrophysics, 98, 1

Mollá M., Ferrini F., Díaz A. I., 1997, The Astrophysical Journal, 475, 519

Monteverde M. I., Herrero A., Lennon D. J., Kudritzki R. P., 1997, The Astrophysical Journal Letters, 474, L107

Pagel B. E. J., 1997, Nucleosynthesis and Chemical Evolution of Galaxies. Cambridge University Press

Pauli W., 1925, Zeitschrift fur Physik, 31, 765

Regan M. W., Vogel S. N., 1994, The Astrophysical Journal, 434, 536

Robles-Valdez F., Carigi L., Peimbert M., 2012, Monthly Notices of the Royal Astronomical Society, 429, 2351

Rogers N. S. J., Skillman E. D., Pogge R. W., Berg D. A., Croxall K. V., Bartlett J., Arellano-Córdova K. Z., Moustakas J., 2022, The Astrophysical Journal, 939, 44

Rosswog S., Sollerman J., Feindt U., Goobar A., Korobkin O., Wollaeger R., Fremling C., Kasliwal M. M., 2018, Astronomy and Astrophysics, 615, A132

Salpeter E. E., 1955, The Astrophysical Journal, 121, 161

Sanders R. L., Shapley A. E., Zhang K., Yan R., 2017, The Astrophysical Journal, 850, 136

Schmidt M., 1959, The Astrophysical Journal, 129, 243

Schönrich R., Binney J., 2009, Monthly Notices of the Royal Astronomical Society, 396, 203

Schönrich R., McMillan P. J., 2017, Monthly Royal Notices of the Royal Astronomical Society, 467, 1154

Schönrich R. A., Weinberg D. H., 2019, Monthly Royal Notices of the Royal Astronomical Society, 487, 580

Siegel D. M., Barnes J., Metzger B. D., 2019, Nature, 569, 241

Smith H. E., 1975, The Astrophysical Journal, 199, 591

Tiede G. P., Sarajedini A., Barker M. K., 2004, The Astronomical Journal, 128, 224

Tinsley B. M., 1979, The Astrophysical Journal, 229, 1046

Toribio San Cipriano L., García-Rojas J., Esteban C., Bresolin F., Peimbert M., 2016, Monthly Royal Notices of the Royal Astronomical Society, 458, 1866

Tsujimoto T., Nishimura N., 2015, The Astrophysical Journal Letters, 811, L10

Urbaneja M. A., Herrero A., Kudritzki R. P., Najarro F., Smartt S. J., Puls J., Lennon D. J., Corral L. J., 2005, The Astrophysical Journal, 635, 311

Vilchez J. M., Pagel B. E. J., Diaz A. I., Terlevich E., Edmunds M. G., 1988, Monthly Royal Notices of the Royal Astronomical Society, 235, 633

Wanajo S., Janka H.-T., Müller B., 2010, The Astrophysical Journal Letters, 726, L15

Williams B. F., Dalcanton J. J., Dolphin A. E., Holtzman J., Sarajedini A., 2009, The Astrophysical Journal Letters, 695, L15

Worthey G., Dorman B., Jones L. A., 1996, The Astronomical Journal, 112, 948

Zaritsky D., Elston R., Hill J. M., 1989, The Astronomical Journal, 97, 97

de Vaucouleurs G., de Vaucouleurs A., Corwin Jr. H. G., Buta R. J., Paturel G., Fouque P., 1991, Third Reference Catalogue of Bright Galaxies

van den Bergh S., 1957, Zeitschrift für Astrophysik, 43, 236

van der Kruit P. C., Searle L., 1981, Astronomy and Astrophysics, 95, 105

van der Marel R. P., Fardal M., Besla G., Beaton R. L., Sohn S. T., Anderson J., Brown T., Guhathakurta P., 2012, The Astrophysical Journal, 753, 8